Xiaoyan ZHANG, Jingqiu CHEN, Yongxiang ZHANG, Chunxia WEI

University of Chongqing

# Numerical Simulation of ESWL with Single-pulse and Dual-pulse Based on 2D Unstructured Grid CE/SE Method

*Abstract. This research focused on the pressure of the single-pulse and dual-pulse of ESWL (Extracorporeal Shock Wave Lithotripsy). And both results were compared and analyzed. Based on the 2D axisymmetric Euler equations and hybrid grids improved CE / SE numerical scheme, the pressure field was simulated in the case of water is the pressure transmission medium. Using the pressure field of shock wave lithotripsy simulated, single-pulse and dual-pulse pressure values near the focus were compared. A Great negative pressure was occurred after the positive pressure near the focus. Furthermore, dual-pulse pressure was about twice of the single-pulse near the focus. The simulation results provided a reliable numerical simulation result for the design and application of ESWL lithotripter.*

*Streszczenie. Badano możliwości jedno- i dwupulsowej litotrypsji (techniki rozbijania kamienia nerkowego). Przedstawiono model matematyczny w wodą jako medium przenoszenia ciśnienia. (Numeryczna symulacja pulsacyjnej metody rozbijania kamienia nerkowego – litotrypsji)*

**Keywords:** ESWL, CE/SE, Unstructured Grid.
**Słowa kluczowe**: litotrypsja, kamień nerkowy.

## Introduction

ESWL (Extracorporeal Shock Wave Lithotripsy), by firing shock waves at the stone [1], which can be broken down into small fragments, for non-invasive surgical trauma and effective stone, is at the forefront of treatment of kidney stones. Although the treatment is non-invasive, both short- and long-term side effects occur. In order to understand and rectify these shortcomings, improving the efficiency of lithotripsy and minimizing tissue damage, become the focus of the process of ESWL. Various researches have been made to clarify mechanism [2,5-7,9] of ESWL and tissue damage[3,4] more than two decades. These studies indicate that the destruction of medical shock wave mechanism, the positive and negative by focusing and the cavitation in ESWL is a crucial element in the stone comminution process damage stone and the organization played a pivotal role. Generally used in clinical shock wave frequency is 1~2Hz, but small enough to make stone discharge from the urethra need to impact the number of generally 1500 to 3000, thereby increasing the efficiency of the stone comminution process is very necessary.

Clinical use of the current models by the type of shockwave source they utilize can be divided into three types: Electro-hydraulic, Electro-mechanical, Acoustic lens focusing and piezoelectric, in addition to laser-and micro-explosion, etc.. Electro-hydraulic is used in the first and the most popular kind of ESWL. The initial shock wave is generated by the discharge across a spark gap located at the first focus of ellipsoidal reflector. Since the reflector is not a completed enclosure, part of the shock wave is reflected towards the second focal point[8], which can break down the stone into small fragments. In this study, we will focus on the evolution of the pressure of the single-pulse and dual-pulse Electro-hydraulic Dornier HM3 lithotripter. The computational domain of the lithotripter used in this study is dealt with an axisymmetrical rotational ellipsoid.

The space-time conservation element and solution element method (CE/SE) is used in this paper. This approach, proposed to solve the problem of hyperbolic conservation equations, is pioneered by Chang S C [16]. The method, improved and optimized by Zhang Zeng-Chan[14], Zhang Yong-Xiang[10,11], has been widely used on the two-dimensional, three-dimensional Euler, N-S equation problems. The governing equations are discrete by an improved grid-based hybrid CE/SE method.

## Theoretical analysis

2D conservation governing differential equations

(1)
$$\frac{\partial \mathbf{Q}}{\partial t} + \frac{\partial \mathbf{F}(\mathbf{Q})}{\partial x} + \frac{\partial \mathbf{G}(\mathbf{Q})}{\partial y} = \mathbf{B}(\mathbf{Q})$$

Where: Q - the vectors of the basic variables based on conservation forms, F(Q) - the numerical fluxes in X direction, G(Q) - the numerical fluxes in X direction, B(Q) - the source terms of governing equations, F(Q)、G(Q) and B(Q) - the functions of the basic variables Q.

$$\mathbf{Q} = \begin{Bmatrix} Q_1 \\ Q_2 \\ \vdots \\ Q_m \end{Bmatrix}; \ \mathbf{F} = \begin{Bmatrix} F_1 \\ F_2 \\ \vdots \\ F_m \end{Bmatrix}; \ \mathbf{G} = \begin{Bmatrix} G_1 \\ G_2 \\ \vdots \\ G_m \end{Bmatrix}; \ \mathbf{B} = \begin{Bmatrix} B_1 \\ B_2 \\ \vdots \\ B_m \end{Bmatrix}$$
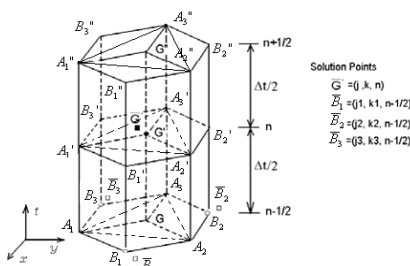


Fig.1. Definition of conservation element and solution element

The unstructured grid of CE/SE 2D schemes which can be applied to any irregular computational domain based on the structured grid of Chang S.C, are designed. The two-dimensional computational domains are divided into connecting but non-overlapping triangular or quadrilateral mesh grids. The design of conservation elements and solution elements as shown in figure1，solution elements are pentahedron $A_1A_2A_3A_3"A_2"A_1"$ adding hexagon $A_1B_3A_2B_2A_3B_1$ and conservation elements are octahedron $A_1B_3A_2B_2A_3B_1B_1'A_3'B_2'A_2'B_3'A_1'$ in the case of triangle meshes. Figure 2 is the projection on the plane: $A_i$, $G$, $B_i$ and $\overline{G}$ are the grid nodes, geometric center, adjacent unit centroids and computational node of solving units, respectively. Generally, the centroid $\overline{G}$ of polygon $A_iB_i$, contained the values of all basic variables, and grid node G are different. As shown in Figure 1 points $A_i"$ ($A_i'$), $B_i"$ ($B_i'$), and $G"$ ($G'$) are on the time level $n+1/2$ (n) with their spatial

projections on the time level $n-1/2$, respectively, being the points $A_i$, $B_i$ and $G$ that are depicted in Figure 2 $(x_j, y_k, t^n)$ and $(x_{j_i}, x_{k_i}, t^{n-1/2})$, respectively, are the coordinates of the mesh point $G'(j,k,n)$ and $A_i(j_i, k_i, n-1/2)$, where $i=1,2,3$ for triangular elements.
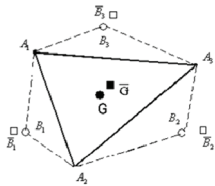


Fig.2. The conservation and solution element of triangular grid

The design of CE/SE method is to unify space and time and treat them as a single entity. Let $x_1=x, x_2=y, x_3=t$ be considered as the coodinates of a three-dimentional Euclidean space $E_3$. By using Gauss' divergence theorem in the space-time $E_3$, it can be shown that equation (1) is the differential form of the integral convervation law.

$$\text{(2)} \qquad \oint_{S(V)} H_m ds = \oint_V B_m dV$$

Here $S(V)$ is the boundary of an arbitrary space-time region $V$ in $E_3$. $H_m = (F_m, G_m, Q_m)$, m=1,2,3,4, is a current density vector in $E_3$.

For $\forall(x,y,t) \in SE(j,k,n)$, let $Q_m(x,y,t)$, $F_m(x,y,t)$ and $G_m(x,y,t)$ be approximated by $Q_m^*(x,y,t;j,k,n)$, $F_m^*(x,y,t;j,k,n)$ and $G_m^*(x,y,t;j,k,n)$ which are employed by first-order Taylor series expansion; let $B_m(x,y,t)$ be approximated by $B_m^*(x,y,t;j,k,n)$ which are employed by zero-order Taylor series expansion.

Note that, by their definitions $F_m(x,y,t)$, $(F_{mx})_{j,k}^n$, $(F_{my})_{j,k}^n$ and $G_m(x,y,t)$, $(G_{mx})_{j,k}^n$, $(G_{my})_{j,k}^n$ are functions of $(Q_m)_{j,k}^n$, $(Q_{mx})_{j,k}^n$, $(Q_{my})_{j,k}^n$, m=1,2,3,4.

Substituting $Q_m = Q_m^*(x,y,t;j,k,n)$, $F_m = F_m^*(x,y,t;j,k,n)$, $G_m = G_m^*(x,y,t;j,k,n)$ and $B_m = B_m^*(x,y,t;j,k,n)$ into equation (2), it has

$$\text{(3)} \qquad (Q_{mt})_{j,k}^n = (B_m)_{j,k}^n - (F_{mx})_{j,k}^n - (G_{my})_{j,k}^n$$

Thus $(Q_{mt})_{j,k}^n$ are is a function of $(Q_m)_{j,k}^n$, $(Q_{mx})_{j,k}^n$, $(Q_{my})_{j,k}^n$, m=1,2,3,4. From this result, it can conclude that only independent discrete variables needed to be solved for in the unstructured grid CE/SE 2D schemes are $(Q_m)_{j,k}^n$, $(Q_{mx})_{j,k}^n$, $(Q_{my})_{j,k}^n$.

The equation (2) be approximated by

$$\text{(4)} \qquad \oint_{S(CE(V))} H_m^* \cdot ds = \oint_{CE(V)} B_m^* \cdot dV, \quad \forall(j,k,n) \in \Omega$$

The centroid coordinates and area of quadrilateral $GA_iB_iA_{i+1}$ are $(x_{q_i}, y_{q_i})$ and $S_{q_i}$. Then the coordinates $\overline{G}$ can be obtained

$$\text{(5a)} \qquad x_{\overline{G}} = \frac{\sum\limits_i S_{q_i} x_{q_i}}{\sum\limits_i S_{q_i}}$$

$$\text{(5b)} \qquad y_{\overline{G}} = \frac{\sum\limits_i S_{q_i} y_{q_i}}{\sum\limits_i S_{q_i}}$$

The normal direction of the quadrilateral $B_i A_{i+1} A_{i+1}' B_i'$ is

$$s_{B_i A_{i+1} A_{i+1}' B_i'} = \frac{\Delta t}{2}(y_{B_i} - y_{A_{i+1}}, x_{A_{i+1}} - x_{B_i}, 0)$$

The centroid is

$$(x_p, y_p, t_p) = \left( \frac{x_{A_{i+1}} + x_{B_i}}{2}, \frac{y_{A_{i+1}} + y_{B_i}}{2}, t^n - \frac{\Delta t}{4} \right)$$

The flux leaving CE(j,k,n) through $B_i A_{i+1} A_{i+1}' B_i'$ is

$$R_{B_i}^{(1)} = \frac{\Delta t}{2}(y_{B_i} - y_{A_{i+1}})\{(F_m)_{j_i,k_i}^{n-1/2} + ((x_{A_{i+1}} + x_{B_i})/2 - x_{\overline{B_i}})(F_{mx})_{j_i,k_i}^{n-1/2}$$
$$+ ((y_{A_{i+1}} + y_{B_i})/2 - y_{\overline{B_i}})(F_{my})_{j_i,k_i}^{n-1/2} - \frac{\Delta t}{4}(F_{mt})_{j_i,k_i}^{n-1/2}\}$$
$$+ \frac{\Delta t}{2}(x_{A_{i+1}} - x_{B_i})\{(G_m)_{j_i,k_i}^{n-1/2} + ((x_{A_{i+1}} + x_{B_i})/2 - x_{\overline{B_i}})(G_{mx})_{j_i,k_i}^{n-1/2}$$
$$+ ((y_{A_{i+1}} + y_{B_i})/2 - y_{\overline{B_i}})(G_{my})_{j_i,k_i}^{n-1/2} - \frac{\Delta t}{4}(G_{mt})_{j_i,k_i}^{n-1/2}\}$$

Similarly, The flux leaving CE(j, k, n) through $B_i A_i A_i' B_i'$ is

$$R_{B_i}^{(2)} = \frac{\Delta t}{2}(y_{A_i} - y_{B_i})\{(F_m)_{j_i,k_i}^{n-1/2} + ((x_{A_i} + x_{B_i})/2 - x_{\overline{B_i}})(F_{mx})_{j_i,k_i}^{n-1/2}$$
$$+ ((y_{A_i} + y_{B_i})/2 - y_{\overline{B_i}})(F_{my})_{j_i,k_i}^{n-1/2} - \frac{\Delta t}{4}(F_{mt})_{j_i,k_i}^{n-1/2}\}$$
$$+ \frac{\Delta t}{2}(x_{B_i} - x_{A_i})\{(G_m)_{j_i,k_i}^{n-1/2} + ((x_{A_i} + x_{B_i})/2 - x_{\overline{B_i}})(G_{mx})_{j_i,k_i}^{n-1/2}$$
$$+ ((y_{A_i} + y_{B_i})/2 - y_{\overline{B_i}})(G_{my})_{j_i,k_i}^{n-1/2} - \frac{\Delta t}{4}(G_{mt})_{j_i,k_i}^{n-1/2}\}$$

The flux leaving CE(j,k,n) through $GA_iB_iA_{i+1}$ is

$$R_{B_i}^{(3)} = -S_{q_i}\{(Q_m)_{j_i,k_i}^{n-1/2} + (x_{q_i} - x_{\overline{B_i}})(Q_{mx})_{j_i,k_i}^{n-1/2} + (y_{q_i} - y_{\overline{B_i}})(Q_{my})_{j_i,k_i}^{n-1/2}\}$$

The flux leaving CE(j,k,n) through three interfaces associated with point $B_i$ is

$$\text{(6)} \qquad R_{B_i} = R_{B_i}^{(1)} + R_{B_i}^{(2)} + R_{B_i}^{(3)}$$

Where: $i=1,2,3$, $A_4 = A_1$ for triangular elements.

The area normal direction of the interface associated with point $G$ is

$$s_G = \left(0, 0, \sum_i S_{q_i}\right)$$

The centroid is

$$(x_p, y_p, t_p) = (x_{\overline{G}}, y_{\overline{G}}, t^n)$$

The flux leaving the interface is

$$\text{(7)} \qquad R_G = \sum_i S_{q_i} \cdot (Q_m)_{j,k}^n$$

The Integration of $B_m^*$ is

$$\text{(8)} \qquad E_B = \oint_{CE(V)} B_m^* dxdydt = \frac{\Delta t}{2}\{S_{A_i}(B_m)_{j,k}^n + \sum_i (S_{B_i} \cdot (B_m)_{j_i,k_i}^{n-1/2})\}$$

Substituting equation (6), (7) and (8) into equation (4), it can be obtained

$$\text{(9)} \quad (Q_m)_{j,k}^n - \frac{\Delta t}{2} \frac{S_{A_i}}{\sum\limits_i S_{q_i}}(B_m)_{j,k}^n = \frac{1}{\sum\limits_i S_{q_i}}\left\{ \frac{\Delta t}{2}\sum_i (S_{B_i} \cdot (B_m)_{j_i,k_i}^{n-1/2}) - \sum_i R_{B_i} \right\}$$

Equation (9) is the major format to discrete $(Q_m)_{j,k}^n$ based on the unstructured grid.

Where: $S_{A_i}$ - the area of the solving unit $(A_1A_2A_3)$, $S_{B_i}$ - the triangular area $(A_iB_iA_{i+1})$ which is made up of the adjacent unit centroid and the adjacent edges of the solving unit, $S_{q_i}$ - the quadrilateral area $(A_iB_iA_{i+1}G)$ which is made up of the adjacent unit centroid, the adjacent edges of the solving unit and the centroid of the solving unit, $x_{Ai}$, $y_{Ai}$ - the coordinates for the solving unit, $x_{Bi}$, $y_{Bi}$ - the coordinates for the adjacent unit of the solving unit, $x_{\overline{B_i}}$, $y_{\overline{B_i}}$ - the centroid coordinates for the adjacent polygonal unit of the solving unit, where $i=1,2,3$ is for triangular elements.

There must be two major discrete equations solving $(Q_{mx})_{j,k}^n$ and $(Q_{my})_{j,k}^n$ because the spatial gradients $(Q_{mx})_{j,k}^n$

and $\left(Q_{my}\right)^n_{j,k}$ need to be solved as independent discrete variables in the unstructured grid 2D CE/SE schemes. In this paper central difference method in the unit is used to obtain the discrete equations of spatial gradient.

(10a) $$(Q_{mx})^n_{j,k} = \frac{1}{n}\sum_{i=1}^{n}(Q_{mx}^{(i)})^n_{j,k}$$

(10b) $$(Q_{my})^n_{j,k} = \frac{1}{n}\sum_{i=1}^{n}(Q_{my}^{(i)})^n_{j,k}$$

Where: $i = 3$, for triangular elements.

Equation (10) must be modified as following for obvious discontinuous

(11a) $$(Q_{mx})^n_{j,k} = \frac{1}{\omega}\sum_{i=1}^{n}\{(\prod_{l=1,l\neq i}^{n}\theta_{ml})^\alpha \cdot (Q_{mx}^{(i)})^n_{j,k}\}$$

(11b) $$(Q_{my})^n_{j,k} = \frac{1}{\omega}\sum_{i=1}^{n}\{(\prod_{l=1,l\neq i}^{n}\theta_{ml})^\alpha \cdot (Q_{my}^{(i)})^n_{j,k}\}$$

Here :

$$\omega = \sum_{i=1}^{n}\{(\prod_{l=1,l\neq i}^{n}\theta_{ml})^\alpha\}$$

$$\theta_{ml} = \sqrt{\{(Q_{mx}^{(l)})^n_{j,k}\}^2 + \{(Q_{my}^{(l)})^n_{j,k}\}^2}$$

where: $n = 1,2,3$, for triangular elements.

The equations (9)、(10)or (9)、(11) are the major format to discrete based on the unstructured grid.

A conservation element can derive a major discrete equation at each grid node by designing unstructured grid. Meanwhile, all independent variables can be solved by the basic variable and its spatial gradients which obtained by Taylor series expansion and central difference method. This numerical scheme is adapted to simulate complex boundary，especially the multi-dimension and higher order accuracy.

Solid and outer boundary conditions are required for the modeling. Taking a triangle mesh for example, the horizontal direction solid boundary is shown as figure 3. Non nodes locate on the boundary because the information of nodes are solved on the centroid while not on the element nodes. Fictitious nodes (E) are added to the domain with values taken from their image counterpart(G).
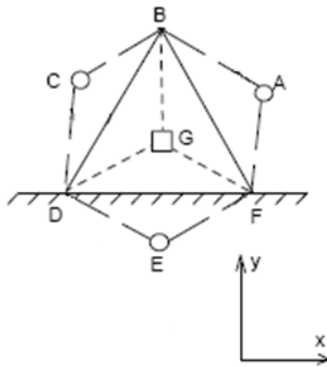


Fig.3. A sketch for boundary cell

Here :

(12a) $$\begin{cases}\left(Q_m\right)_E = \left(Q_m\right)_G & m \neq 3 \\ \left(Q_m\right)_E = -\left(Q_m\right)_G & m = 3\end{cases}$$

(12b) $$\begin{cases}\left(Q_{mx}\right)_E = \left(Q_{mx}\right)_G & m \neq 3 \\ \left(Q_{mx}\right)_E = -\left(Q_{mx}\right)_G & m = 3\end{cases}$$

(12c) $$\begin{cases}\left(Q_{my}\right)_E = -\left(Q_{my}\right)_G & m \neq 3 \\ \left(Q_{my}\right)_E = \left(Q_{my}\right)_G & m = 3\end{cases}$$

The first-order extrapolation method is used tomodel outer boundary conditions.

(13) $$\left(Q_m\right)_E = \left(Q_m\right)_G ; \left(Q_{mx}\right)_E = 0 ; \left(Q_{my}\right)_E = 0$$

### Source terms

The Newton's iterative is used in the source terms for the coupling of $H_m$ and $Q_m$ in equation (2). Simplifying equation (9) as following:

(14) $$\mathbf{Q} - \mathbf{H}(\mathbf{Q})\frac{\Delta t}{2}S_b = \mathbf{Q}_0$$

Here $Q_0$ is the known values of The previous time layer on the right side of equations (9). Q and H(Q) are vectors of equation (2). The Newton's iterative is used in equation (14).

$$\mathbf{Q}^{(i+1)} = \mathbf{Q}^{(i)} - \left(\frac{\partial \mathbf{\Phi}}{\partial \mathbf{Q}}\right)^{-1}\left[\mathbf{\Phi}(\mathbf{Q}^{(i)}) - \mathbf{Q}_0\right]$$

Where: i - the number of iterations. Let

$$\mathbf{\Phi}(\mathbf{Q}) = \mathbf{Q} - \mathbf{H}(\mathbf{Q})\frac{\Delta t}{2}S_b$$

The values iterating 2~3 times can converges to the final solution while the initial value is taken in the vicinity of the final solution. Therefore, the values without source terms are used as the initial conditions of the Newton's iterative in this paper.

### Numerical methods

The simulation and in vitro physical studies of ESWL, which use water as a pressure transmission medium, can be simplified as the process of underwater shock wave focusing due to the similarity between acoustic impedance for body soft tissue and water. The 2D axisymmetric Euler governing equations for inviscid, compressible, non heat conduction and adiabatic conditions are:

(15) $$\frac{\partial Q_m}{\partial t} + \frac{\partial F_m}{\partial x} + \frac{\partial G_m}{\partial r} = H_m$$

where：

$$Q_m = \begin{Bmatrix}\rho \\ \rho u \\ \rho v \\ \rho E\end{Bmatrix} ; F_m = \begin{Bmatrix}\rho u \\ \rho u^2 + p \\ \rho uv \\ (\rho E + P)u\end{Bmatrix} ; G_m = \begin{Bmatrix}\rho v \\ \rho uv \\ \rho v^2 + P \\ (\rho E + P)v\end{Bmatrix} ; H_m = -\frac{1}{r}\begin{Bmatrix}\rho v \\ \rho uv \\ \rho v^2 \\ (\rho E + P)v\end{Bmatrix}$$

Here t is the time，x is the axial coordinate，r is the Radial coordinate， $\rho$ is the flow density, u is the x-axis direction of velocity component, v is the r-axis direction of velocity component, p is the flow pressure，E is defined as $E = \frac{p}{(\rho(\gamma - 1))} + 0.5(u^2 + v^2)$, γ is ratio of specific heats.

Figure 4 is the schematic of electrohydraulic crusher. The reflector is a symmetric fragment of rotation ellipsoid. The frequently-used reflector is slightly less than half of the rotation ellipsoid. Its basic mechanics are that the energy released at the focus of rotation ellipsoid, and it spreads in the form of spherical shock wave. One part of the spherical wave translates to reflected wave encountering the reflector. The focus tends to the second geometrical focus area. The stone in this focus area crushed after repeated bombardment by shock wave.
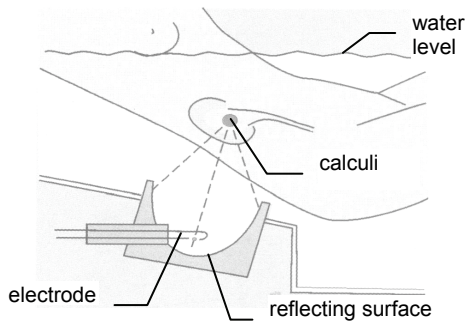
Fig.4. Electro-hydraulic lithotripter focusing diagram

## The numerical simulation of single-pulse lithotripter

The diagram of the electrohydraulic lithotripter based on Dornier HM3 with relevant dimensions is shown in Figure 4. The Computational domain, employed a semi-ellipsoidal reflector with semi-major axis a=138.1mm, semi-minor b=78.0mm, half-focal length c=114.0mm, and half-depth h=12.5mm, is shown in Figure 5. The wave reflects from the ellipsoidal surface AE. The initial pressure at the first focus is 12.0MPa, the rest is full of water with pressure 0.1MPa, density 1063.55kg/m3 and isentropic index n=7.15.

Figure 5 shows the computational domain: axis of symmetry AB=300mm, Outlet BC=120mm , CD=250mm and DE=40.42mm. The number of grid cells and nodes in the computational domain is 84906 and 42927. The length of grid is 1mm. The following boundary conditions are required for this paper: inviscid reflecting boundary conditions at the solid boundary(AE), simple extrapolation at the outer edge of the domain(DE,CD,BC) and no penetration boundary condition at the axis of symmetry(AB).
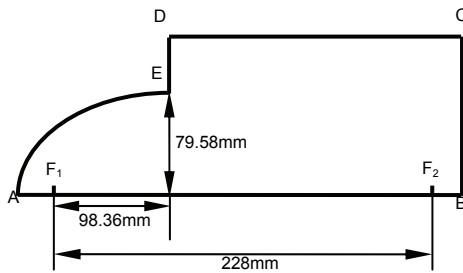


Fig.5. Computational domain of ESWL with single pulse

The isobar figures of single-pulse lithotripter are simulated as shown in Fig.4 based on the2D unstructured grid CE/SE method. In order to compare with the actual device, computing results of upper half plane are copied to lower half plane symmetrically. In this way, a complete meridian plane diagram is obtained. Figure 6(a)~(d) illustrates the pressure contours (140μs、150μs、175μs、200μs after the shock wave generated).



(a) $t = 140 \mu s$      (b) $t = 150 \mu s$



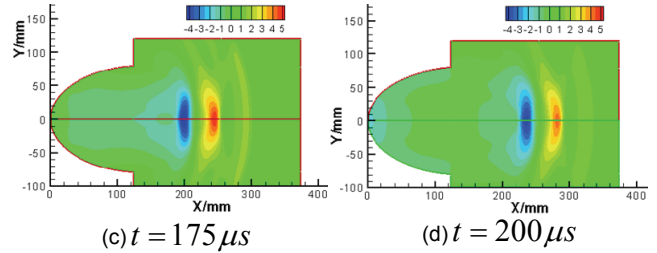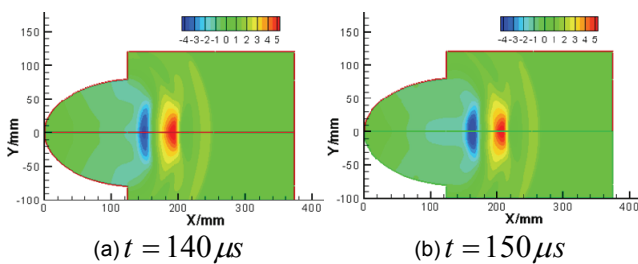(c) $t = 175 \mu s$      (d) $t = 200 \mu s$

Fig.6. The pressure field with the single pulse inside an electro-hydraulic lithotripter

As seen in this series of pictures, the blue and the red lines respectively represent minimum and maximum pressures. The initial shock wave is generated by the discharge across a spark gap located at the first focus of the ellipsoidal reflector (see Figure 6(a) ). Part of the shock wave is reflected because the reflector is not a complete enclosure. While, the reflected wave with the initial wave transmits and converges to the second focus. A diffraction shock wave is produced at the peak of the reflector where the negative pressure is appeared along with the initial wave transmitting and converging to the second focus.

Figure 7 illustrates the computational domain of this paper for the dual-pulse lithotripter. Here, AC、DB is the ellipsoid, two focuses respectively are F1、F2 and F3 is the common focus of two public ellipsoids. The initial pressure at the focuses F1 and F2 are 12.0MPa. The number of grid cells and nodes in the computational domain is 84906 and 42927. Other conditions are the same as the single-pulse.
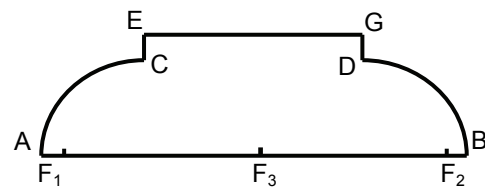


Fig.7. Computational domain of ESWL with dual-pulse

Figure 8(a)~(d) illustrates the pressure contours (140μs、150μs、175μs、200μs after the shock wave generated) of dual-pulse lithotripter.



(a) $t = 140 \mu s$      (b) $t = 150 \mu s$



(c) $t = 175 \mu s$      (d) $t = 200 \mu s$
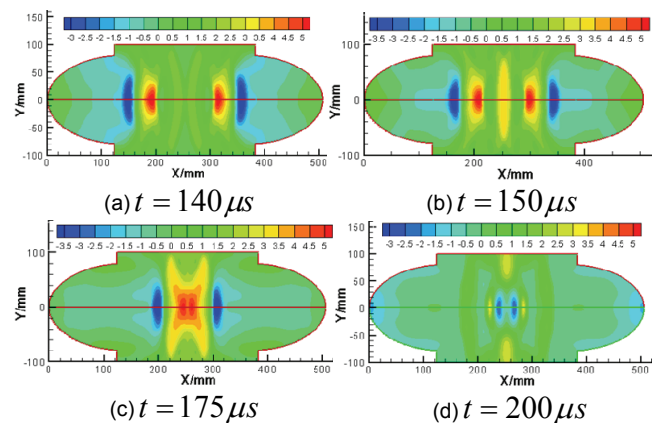
Fig.8. The pressure field with the dual-pulse inside an electro-hydraulic lithotripter

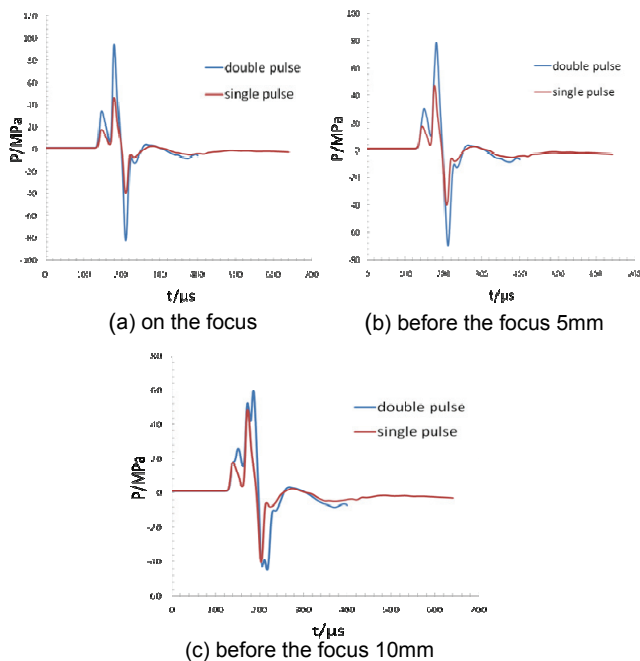(a) on the focus     (b) before the focus 5mm



(c) before the focus 10mm

Fig.9. The Pressure Comparison of he single pulse and dual-pulse lithotripter

As seen in this series of pictures, the blue represents minimum pressure and the red represents maximum one. The pressure between dual-pulse and single-pulse is the same before the incident wave does not encounter. The incident waves of two focuses are meeting at 140µs. Then, the incident waves, reflected waves and diffraction waves overlap and converge to the center by a convex curve into a concave one.

Figure 9 demonstrates the pressure comparison of underwater shock wave focusing between single-pulse and dual-pulse. Figure 9(a)~(c) respectively illustrates the pressure changing with time on the focus, 5mm on the front of focus, 10mm on the front of focus, 5mm on the back of focus and 10mm on the back of focus.

Table 1: The peak pressure on the front of focus (-), on the focus(0), on the back of focus (+) between single-pulse and dual-pulse lithotripter

|  |  | -10mm | -5mm | 0 | +5mm | +10mm |
|---|---|---|---|---|---|---|
| single-pulse | positive (MPa) | 48.8 | 47.8 | 47 | 46.1 | 45.2 |
|  | negative (MPa) | -40.5 | -40.0 | -39.5 | -39.1 | -38.8 |
| dual-pulse | positive (MPa) | 59.3 | 78.6 | 94.4 | 78.8 | 52.4 |
|  | negative (MPa) | -42.4 | -70.0 | -82.8 | -69.1 | -42.0 |

The following conclusions can be summarized from Figure 9 and table 1:

(1) The maximum positive (78.6MPa) and negative pressure (-70.0MPa) of dual-pulse lithotripter 5mm around of focus occur at $180\mu s$ and $210\mu s$. While, the maximum positive (47.8MPa) and negative pressure (-40.0MPa) of single-pulse lithotripter occur at $176\mu s$ and $207\mu s$.

(2) The maximum positive (94.4MPa) and negative pressure (-82.8MPa) of dual-pulse lithotripter on the focus occur at $180\mu s$ and $210\mu s$. While, the maximum positive

(47MPa) and negative pressure (-39.5MPa) of single-pulse lithotripter occur at the same time.

(3) The maximum positive (59.3MPa) and negative pressure (-42.4MPa)of dual-pulse lithotripter 10mm around of focus occur at $186\mu s$ and $206\mu s$. While, the maximum positive (48.8MPa) and negative pressure (-40.5MPa) of single-pulse lithotripter occur at $173\mu s$ and $203\mu s$.

As shown in Table 1, the pressure of dual-pulse lithotripter is about 1.5 times the single pulse for 5mm and 10 mm around the focus; While, the pressure of dual-pulse lithotripter is twice the single pulse on the focus. The interval between the maximum positive and negative pressure is about $30\mu s$. The pressure on the focus is maximal compared with other four locations. is natural considering the symmetry of the structure of dual-pulse ESWL.

**Discussion**

The focusing field of the single-pulse and dual-pulse of ESWL(Extracorporeal Shock Wave Lithotripsy) was simulated by CE/SE method. The pressure both of single-pulse and dual-pulse at the focus, before 5mm and 10mm were compared. The dual-pulse maximum pressure generated at the second geometry focus. The maximum tension and compression value of dual-pulse is almost two times comparing with the value of single-pulse. But it decreases to about 1.5 times at 10mm. The result shows that it is much more efficient comparing dual-pulse with single-pulse close to the focus. All of this provides a reliable numerical simulation result for manufacture and clinical application of ESWL.

Although there is no negative pressure in the initial conditions，the negative pressure gradually produces and increases in the process of focusing by the diffraction and reflection of the reflector, while the negative peak can reach -70.0MPa. The negative pressure is tension, which causes the cavitation occurred in water. What needs to be explained is that the numerical simulation theoretical model is continuous and uniform. And it does not contain micro-bubbles or impurities particulate. It means that the negative pressure generated by shock wave focus will lead to cavitation even in completely pure water. It always needed hundreds of times discharge bombarding in the clinical treatment. the repeated alternating of positive and negative pressure (compression and tension) will not only crush the stone, but the human tissue will also be damaged. Since the mechanical properties of bile is closer to the properties of water than kidney, and inevitably contains tiny bubbles and impurities. Cavitation is more easier occur in bile of the process of shock wave focusing. The results explain that major injuries occur more frequently in comminuting gallstone than kidney stone in the clinical observation. The pressure and cavitation should not be ignored In the design of electrohydraulic ESWL machine and clinical application. The void fraction will be added to the Euler equation to study the bubble cloud in the next step.

REFERENCES
[1] Brennen C E. Cavitation and Bubble Dynamics. *Oxford University Press*, New York/ Oxford, 1995
[2] Chaussy C., Brendel W., Schmiedt E. Extracorporesally induced destruction of kidney stones by shock waves. *Lancet*, 207(1980), No.2, 1265~1268
[3] Delius M., Lithotripsy. *Ultrasound Med Biol*, 26(2000), 55~58
[4] Delius M., Medical applications and bioeffects of extracorporeal shock waves. *Shock Waves*, 56(1994), No.4, 55~72

[5] Tanguay M. Computation of bubbly cavitating flow in shock wave lithotripsy, *California: California Insitute of Technology*, 1(2004)

[6] Wolfgang Eisenmenger. The mechanisms of stone fragmentation in ESWL. *Ultrasound in Medicine & Biology*, 27(2001), No.5, 683~693

[7] Zhong P, Preminger GM. Mechanisms of differing stone fragility in extracorporeal shock wave lithotripsy. *J Endourol*, 8(1994), 163~8

[8] Zhang Yong-Xiang, Chen Jing-Qiu, Deviation of the Factual Focus of Spherical Piezoelectric ESWL from the Spherical Center, *Chinese Journal of Biomedical Engineering*, 27(2007), No.2, 177~181

[9] Chen Jing-Qiu, WEI Chun-Xia, Studies on Mechanical Mechanism about Stone C omminution and Tissue Trauma in Extra Corporeal Shock Wave Lithotripsy, *Advances in Mechanics*, 37(2007), No.4, 590~605

[10] Zhang Yong-xiang CHEN Jing-qiu, Numerical simulation of 2-D dam-break wave by using conservation element and solution element method, *Journal of Hydraulic Engineering*, 36(2005), No.10, 1224-1229

[11] Chen Jing-qiu, Zhang Yong-xiang, Wei Chun-xia, Numerical simulation of propagation diffraction and reflection of 2-D dam-break wave, *Journal of Hydraulic Engineering*, 36(2005), No.5, 569-574

[12] Chang S C. The Method of Space-Time Conservation Element and Solution Element - A New Approach for Solving the Navier-Stokes and Euler Equations. *Journal of Computational Physics*, 119(1995), No.2, 295~324

[13] Chang Sin-Chung,Wang Xiao-Yen and To Wai-Ming. Application of the Space–Time Conservation Element and Solution Element Method to One-Dimensional Convection–Diffusion Problems. *Journal of Computational Physics*, 165(2000), No.1, 189-215

[14] Zhang Zeng-Chan, John Yu S. T. and Chang Sin-Chung. A Space-Time Conservation Element and Solution Element Method for Solving the Two- and Three-Dimensional Unsteady Euler Equations Using Quadrilateral and Hexahedral Meshes, *Journal of Computational Physics*, 175(2002), No.1, 168-199

[15] Lim Young-II, Chang Sin-Chung and Jorgensen Sten Bay. A novel partial differential algebraic equation (PDAE) solver: iterative space–time conservation element/solution element (CE/SE) method. *Computers & Chemical Engineering*, 28(2004), No.8, 1309-1324

[16] Muller M, Stosswellenfokusierung in Wasser, *Dissertation der RWTH Aachen, Germany,* 1988

***Authors***: *Dr Zhang Xiaoyan, Chongqing University, Department of Engineering Mechanics, E-mail: zxyxbb@yahoo.com.cn; Prof. Dr Chen Jingqiu, Chongqing University, Department of Engineering Mechanics, E-mail: jqchen@cqu.edu.cn; Dr Zhang Yongxiang, Department of Engineering Mechanics, E-mail: yxzh@cqu.edu.cn; Dr Wei Chunxia, Department of Engineering Mechanics, E-mail: xwei@cqu.edu.cn.*